

Interrelationship of in Situ Growth Stress Evolution and Phase
Transformations in Ti/W Multilayered Thin Films

Gregory B. Thompson – The University of Alabama
et al.

Deposited 11/12/2018

Citation of published version:

Li Wan, et al. (2016): Interrelationship of in Situ Growth Stress Evolution and Phase Transformations in Ti/W Multilayered Thin Films. *Applied Physics Letters*, 119(24).
DOI: <https://doi.org/10.1063/1.4954687>

Interrelationship of *in situ* growth stress evolution and phase transformations in Ti/W multilayered thin films

Li Wan, Xiao-xiang Yu, Xuyang Zhou, and Gregory Thompson^{a)}

Department of Metallurgical Engineering, The University of Alabama, Tuscaloosa, Alabama 35487-0202, USA

(Received 12 July 2015; accepted 8 June 2016; published online 24 June 2016)

This paper addresses the *in situ* growth stress evolution and phase transformation of bcc to hcp Ti in Ti/W multilayered thin films. A series of equal layer thicknesses from 20 nm to 1 nm were deposited. As the bilayer thickness reduced, the overall film stress became less compressive until the Ti transformed from hcp (at the larger layer thicknesses) to bcc in the 1 nm/1 nm multilayer. The pseudomorphic bcc stabilization resulted in a recovery of the compressive stress to values near that for the bulk phase stabilized for the 5 nm/5 nm multilayer. A discernable change in stress slope was noted for the bcc to hcp Ti transition as a function of Ti layer thickness. The stress states for each film, during film growth, are rationalized by the lattice matching of the phase with the growth surface. These results are coupled to a molecular dynamics deposition simulation which revealed good agreement with the experimentally observed transformation thickness. Published by AIP Publishing. [<http://dx.doi.org/10.1063/1.4954687>]

I. INTRODUCTION

Phase transformations of materials in the nanometer regime are often serendipitously discovered.^{1–3} Multilayered thin films are an ideal architecture to study such length scale dependent phase transformations since these materials exhibit large interfacial-to-volumetric ratios that can be readily controlled through layer thicknesses. The structural and chemical nature of the interfaces can be easily modified as well through the sequence of deposition of different contact compositions and deposition energies.⁴ During deposition, these thin films experience significant stress states^{5–7} that exceed elasticity limits for their bulk counterparts. Such stress conditions likely control and/or influence the stability of the phases formed within these films.

In general, the prediction of phase transformations in multilayered thin films has been explained using both strain induced transformation concepts^{8,9} and classical thermodynamics.^{10–13} In the former model, the film transforming layer achieves a metastable condition which is associated with a local metastable minimum energy state as the lattice parameter undergoes strain. In the thermodynamic approach,^{10–13} the reduced layer thickness results in the interfacial energy reduction dominating the volumetric energy penalty for the phase transformation. Hence, from a thermodynamic prospective, the change in phase is placing the system at its equilibrium condition considering the balance of the interfacial and volumetric energies. In either case, these strains result in stresses in the film which would change the stabilization energy criteria. For example, Thompson *et al.* reported a transition from hcp to bcc Zr within a series of Zr/Nb multilayers¹¹ and related the transformation to coherency strains within the thermodynamic approach. Other hcp to bcc transformations have also been noted for Ti in Ti/Nb multilayers.^{12,14} In this

system, significant Nb interdiffused into the Ti layers and chemically stabilized the transformation to larger layer thicknesses. The role of stress evolution and its interrelationship to interface intermixing and the thermodynamics of a phase transformation remains a fertile area of research.

The intrinsic stresses generated when a thin film grows will alter the thermodynamic energies of the system and provide a connection between the strain induced and thermodynamic based approaches described above. It is generally accepted that the initial compressive stress at the first stage of growth is a result of the atomic-scale migration into embryonic islands that form to minimize surface area to volumetric energies as the atoms nucleate on the substrate.^{15–17} The subsequent tensile stress originates from the elastic strain associated with the coalescence of these islands to minimize the grain boundary energy. Upon post coalescence of the grains, the stress may retain either a tensile or compressive state depending on the mobility of the adatoms.^{18–21} Elemental films with low atomic mobility, such as Fe, Cr, and Al, tend to retain the tensile condition with continued growth unless acted upon by external stimuli, such as heating the substrate. For films with atoms of higher intrinsic mobility, such as Cu, Nb, and Ti, they exhibit a return to compressive stress in the post coalescence condition. The mechanism of post-coalescence compressive stress is still under discussion.^{22–25}

All of these stresses can be captured by measuring the substrate bending moments creating by the growing film using a laser reflection technique.²⁶ The relations of the film stress and the substrate curvature are given by the Stoney equation²⁷

$$\sigma_f = \frac{E_s}{6(1 - \nu_s)} \frac{t_s^2}{t_f} \left(\frac{1}{R} - \frac{1}{R_0} \right), \quad (1)$$

where σ_f is the film stress, E_s is the Young's modulus of the substrate, ν_s is the Poisson's ratio for the substrate, t_s and t_f are the thicknesses of the substrate and the film, and $1/R$ and

^{a)}Author to whom correspondence should be addressed. Electronic mail: gthompson@eng.ua.edu

$1/R_0$ are measured curvatures of the film before and during/after the deposition. This equation considers the force balance between the substrate and the film. By knowing the Young's modulus and Poisson's ratio of the substrate, as well as detecting the curvature change, the biaxial stress in the film is determined.

Shull and Spaepen²⁸ have applied the measurements of single film stress growth to that of Ag/Cu multilayered films. These stress states were used to deduce atomic mobility¹⁵ of each film on the other, where a tensile state is related to low adatom mobility and compressive state to higher adatom mobility. The interfacial stress of each layer was determined by comparing how the stress changed when one layer grew on the other.²⁸ This type of stress measurement would provide a very interesting diagnostic tool to investigate how phase transformations influence adatom mobility during growth. The authors here have recently used such *in situ* stress measurements to successfully monitor the hcp to bcc Ti transformation in Ti/Nb multilayers.¹⁴ It was observed that Ti initially grew in a tensile condition up to ~ 2 nm where Ti transformed to hcp and the stress reverted to a compressive stress state in the Ti layer.

This research will further those studies by investigating the interrelationship of *in situ* growth stress evolution for a possible Ti phase transformation in Ti/W thin film multilayers. Unlike the prior Ti/Nb multilayers,¹⁴ where the bcc lattice values between β -Ti ($a = 0.327$ nm, extrapolated to room temperature¹⁴) and bcc Nb ($a = 0.330$ nm) are nearly equivalent yielding a coherent interface, the Ti/W system offers a much more strained interface of β -Ti with W ($a = 0.316$ nm). Under such conditions, the stress states should be altered and provided new insights into Ti's stabilization. These results will help to explain how film growth is altered by interfacial energy reduction and strain. This will help bridging our knowledge gaps between strain induced and thermodynamic driven phase transformations.

II. EXPERIMENTAL AND SIMULATION DETAILS

A. Thin films deposition and post-growth characterization

The Ti/W multilayered thin films with equivalent individual layer thicknesses were sputter-deposited from >99.95% pure elemental targets onto [001] Si substrates to a thickness of ~ 200 nm. These films had equivalent layer thicknesses which ranged from 20 nm to 1 nm or bilayers from 40 nm to 2 nm. The base vacuum pressure prior deposition was $< 10^{-8}$ Torr. For sputtering, ultra-high purity argon was flowed as the working gas at 10 standard cubic centimeters per minute flow rate to a pressure of 2 mTorr.

The *in situ* stress evolution during the deposition was monitored using a laser reflection measurement technique with the *k*-Space Associates (kSA[®]) Muti-beam Optic Sensor (MOS). The details about this wafer curvature-based technique can be found elsewhere.²⁶ The deposition rates of Ti and W were determined by dividing the film thickness, measured from X-Ray Reflectivity (XRR)²⁹ and confirmed by the Transmission Electron Microscopy (TEM) cross-sectional micrographs, by the deposition time. XRR was

performed on a X'pert Philips diffractometer operated with Cu K α radiation at 40 kV and 30 mA. The growth rates of Ti and W were 0.029 nm/s and 0.060 nm/s, respectively. X-Ray Diffraction (XRD) was conducted *ex situ* on Bruker Discovery D8 General Area Diffraction Detector Systems (GADDS) with Co K α radiation operated at 40 kV and 35 mA for phase identification of the post deposited films. Selected Area Electron Diffraction (SAED) patterns were also taken from thin plan-view/cross-section foils in the FEI Tecnai F20 (S)TEM. The plan-view foils were prepared by cutting a 3 mm diameter disc from the bulk sample and SiC grinding the disc to be < 100 μ m, followed by dimpling the disc in a Fischione Model 200 Grinder to a thickness of ~ 10 μ m at the bottom of the dimple. The dimpled discs were ion milled using a Gatan 691 Precision Ion Polishing System (PIPS) that utilizes Ar ions to create electron transparent perforations in the dimpled region. The diffraction pattern together with XRD results provided phase identification and preferential growth orientation results. Cross-sectional TEM foils were prepared by Focused Ion Beam (FIB) lift out technique³⁰ with a 5 kV clean up step to reduce any Ga $^{+}$ implantation on the foil surface using the FEI Quanta 3D dual beam FIB-SEM.

B. Simulation method

The experimental results were coupled with a Molecular Dynamics (MD) simulation to provide insights on how the lattice mismatch and elastic strain at the interfaces contribute to the final crystal structure of the thin films. The MD simulations were performed utilizing the LAMMPS code. The monatomic potentials have to be normalized to a unique state instead of being simply combined from the two potentials.³¹ The binary Ti-W embedded atom model (EAM) potential was generated from a developed alloy EAM potential database^{32,33} of sufficient generality with normalized elemental potentials. The in-plane directions of the model were periodic boundary conditions while the out-of-plane (growth) direction was fixed. For the W initial growth layer, $2 \times 2 \times 2$ grains were randomly produced by the Voronoi construction.³⁴ Four regions were created in the model: (1) a fixed region with the atoms in the bottom 1 nm immobile to prevent the movement of the initial W layer by the incident atoms; (2) a temperature region where the incoming atoms interact with the underlayer; (3) an insertion region where the incident Ti atoms at a kinetic energy, E_k , of 1 eV were injected in a normal fashion towards the initial W layer every 1 ps; and (4) a virtual wall region was used to re-sputter the atoms reflected by the W layer with initial kinetic energy E_k to improve the simulation efficiency. It should be noted that for the deposition process, the microcanonical NVE (number, volume, energy) ensemble was first used for all the regions until the canonical NVT (number, volume, temperature) ensemble was introduced for the temperature region to solve the equations of motion for the atoms such that the system temperature was maintained at 300 K. The structures were then fully relaxed for 500 ps after deposition to achieve equilibrium. OVITO software³⁵ was used to visualize the outputs and the results of which will be discussed in Sec. III.

III. RESULTS AND DISCUSSION

A. Phase identification

Similar to what has been observed in the Ti/Nb metallic multilayered thin film system,¹⁴ Ti adopts a bcc structure when it grows sufficiently thin within the Ti/W stacking structure. This stabilization was determined by the XRD and electron diffraction patterns shown in Figs. 1 and 2. As discussed above, this pseudomorphic transition is believed to be the interplay of interfacial energy reduction and strain. In the thermodynamic model,¹⁰ the volumetric energy penalty for the Ti hcp to bcc transformation, ΔG_v , is offset by the interfacial energy reduction, $\Delta\gamma$, for the transformation. Considering a fixed surface area, the bilayer's total free energy change per area, Δg_T , would then be

$$\Delta g_T = 2\Delta\gamma + (\Delta G_v f_{Ti})\lambda, \quad (2)$$

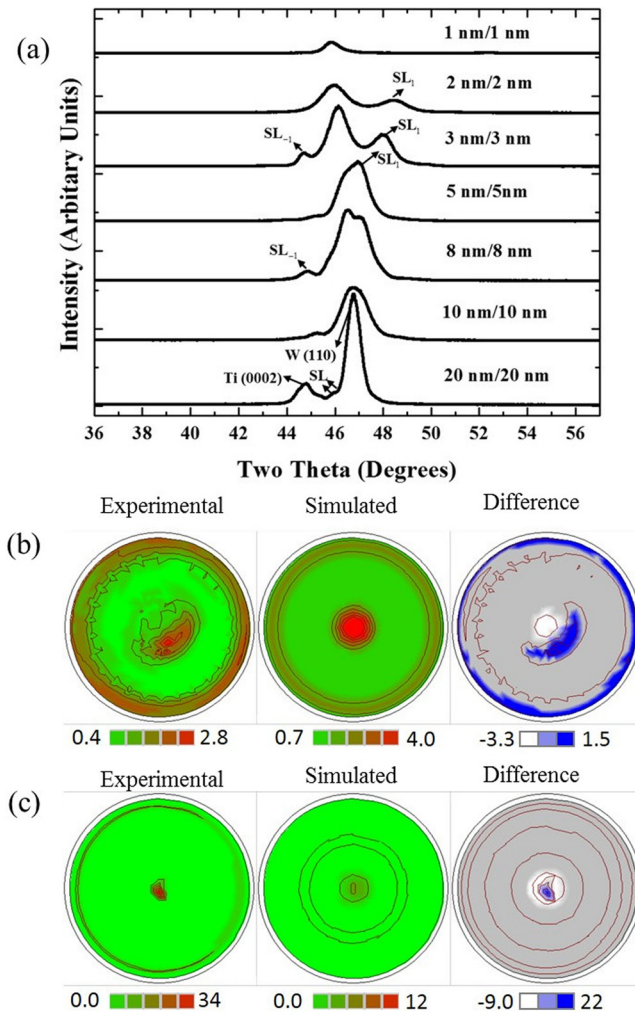


FIG. 1. (a) XRD results of various multilayers listed by their bilayer thicknesses. (b) Pole figure of the Ti/W 1 nm/1 nm multilayer with no prevalent or strong cubic {110} fiber texture observed in the experimental scan. The simulated pole figure and difference pole figure (which is the subtraction of the experimental data from the simulated date) are also provided and labeled. (c) Pole figure of the Ti/W 20 nm/20 nm multilayer confirmed a prevalent {110} texture in the experimental scan with the simulated and difference pole figures to the right of this image. The color scale provides the relative value degree of mismatch in how well aligned the grains are to the {110} texture.

where $\Delta\gamma$ and ΔG_{Ti} have been previously defined above, f_{Ti} is the volume fraction of Ti in the bilayer (0.5, for this film), λ is the bilayer thickness, and the number two is a result of the two interfaces that encapsulate the bilayer.

The XRD results of all the multilayers were shown in Fig. 1(a). For the 20 nm/20 nm Ti/W multilayers, the two intense peaks are indexed as Ti (0002) (44.9° , d-spacing 2.341 Å, ICDD 0020-044-1294) and W (110) (47.1° , d-spacing 2.238 Å, ICDD 00-004-0806) with two close satellite (SL) reflections between these two major peaks. As the bilayer thickness decreased, numerous satellite reflections were generated and these patterns correspond to what is expected for a multilayer superlattice^{36,37} when the coherence length regarding diffraction becomes larger than one deposited bilayer. Under such conditions, epitaxial growth is not mandatory but an orientation relationship between the deposited layers can be sufficient for constructive interference in the growth direction creating these extra SL reflections. Note that the XRD measurements display the out-of-plane reflection³⁸ with peak broadening at smaller bilayer thicknesses. This broadening can be contributed to the distributions of interplanar distances in the growth direction created from the stress in a thinner volume of material and/or interdiffusion between the layers. In 1 nm/1 nm multilayer, a single XRD peak was noted and could suggest the formation of an intermixed alloy film. However, as will be shown in Fig. 2, this 1 nm/1 nm multilayer retained a continuous, layered morphology.

With the continual reduction of the bilayer, a decrease in the XRD reflected intensity, Fig. 1(a), was also noted. This could be contributed to either the particular phase having a loss in crystallinity and/or a shift in texture which lowers the captured intensity in the particular Bragg-Brentano diffraction detector configuration. The high resolution transmission electron microscopy (HRTEM) image in Fig. 2 revealed lattice fringes for both the layers indicating that Ti and W are not vitrified. A series of pole figures, Figs. 1(b) and 1(c), did show a loss of preferential out-of-plane growth alignment for the (110) fiber texture with a decreasing bilayer spacing, which may account for reduction in intensities noted.

Since phase identification using a single XRD peak could be dubious, we have also provided complimentary plan-view electron diffraction where multiple $\{hkl\}$ reflections were observed. Figs. 2(a) and 2(b) are representative plan-view TEM micrographs for the 20 nm/20 nm and 1 nm/1 nm multilayers, respectively. The in-plane grain size for each film varies from ~ 20 to ~ 50 nm. The SAED patterns for each film are shown in Figs. 2(c) and 2(d). In the 20 nm/20 nm Ti/W film pattern (Fig. 2(c)), a distinctive $\{10\bar{1}0\}$ hcp Ti ring is present. However, in the 1 nm/1 nm multilayer, this reflection is absent and only the bcc symmetric reflections are indexed (Fig. 2(d)). The TEM cross section micrographs, Figs. 2(e) and 2(f), reveal a chemically modulated layer structure for each multilayer with relatively smooth and abrupt interfaces. The scanning TEM—High Angle Annular Dark Field (HAADF) image of Fig. 2(f) 1 nm/1 nm clearly confirms a film with continuous and phase separated layers. Unlike a bright field image, which is sensitive to contrast changes from Bragg scattering, contour bends, and thickness

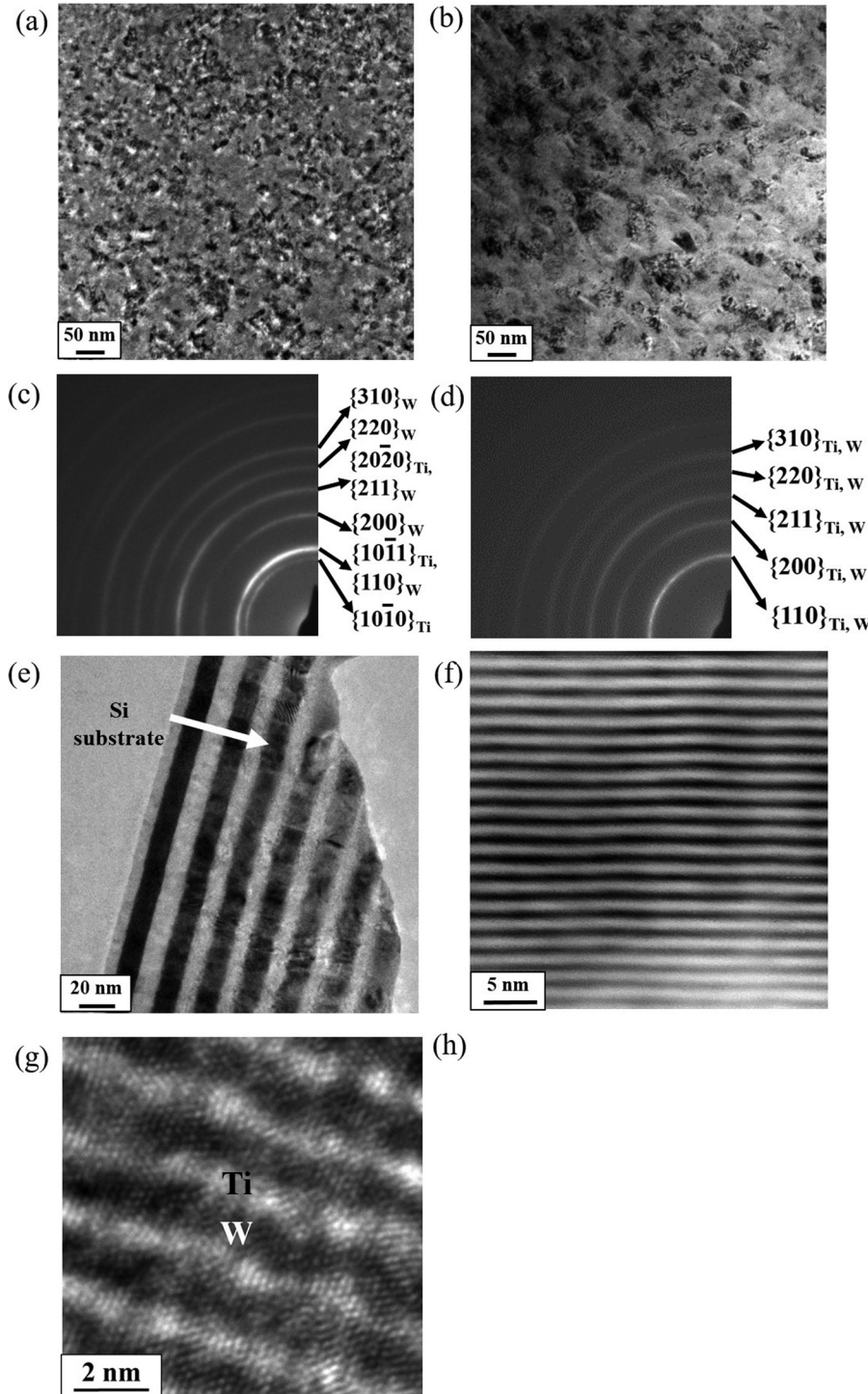


FIG. 2. (a) Plan-view TEM image of 20 nm/20 nm Ti/W multilayer. (b) Plan-view TEM image of 1 nm/1 nm Ti/W multilayer. (c) SAED pattern of 20 nm/20 nm, 10 nm/10 nm, 8 nm/8 nm, 5 nm/5 nm, 3 nm/3 nm, 2 nm/2 nm Ti/W multilayer. (d) The SAED pattern of 1 nm/1 nm Ti/W multilayer. (e) Cross-sectional TEM image of 10 nm/10 nm Ti/W multilayer with an inset of the SAED pattern. The white arrow shows the film exhibits a texture along the layer modulation direction. (f) STEM-HAADF image of 1 nm/1 nm Ti/W multilayer. (g) HRTEM image of 1 nm/1 nm Ti/W multilayer.

fringes, the HAADF collects incoherently scattered electrons whose intensity is directly proportional to nearly the square of the atomic number, $Z^{\sim 2}$. Because of the large difference in atomic number between Ti (22) and W (74), clear chemical imaging differences are readily observed. Even at this very thin layer spacing, distinct contrast from the Ti (dark contrast) and W (bright contrast) is seen suggestive that intermixing through the layers was not significantly present at the interfaces.

Figs. 2(e) and 2(f) are representative cross-sectional TEM micrographs of the 10 nm/10 nm and 1 nm/1 nm Ti/W multilayers. An inset of SAED pattern for the 10 nm/10 nm

film exhibited specific reflections along the layer modulation direction, as highlighted by the white arrow in Fig. 2(e). These reflection could satisfy either the α -hcp/ β -bcc Ti Burgers $\langle 1\bar{1}\bar{2} \rangle_{\alpha}/\langle 111 \rangle_{\beta} | (0001)_{\alpha}/(011)_{\beta}$ ³⁹ or Potter $\langle 11\bar{2}0 \rangle_{\alpha}/\langle 111 \rangle_{\beta} | (\bar{1}011)_{\alpha}/(011)_{\beta}$ ⁴⁰ and could not be definitively determined.

B. *In situ* stress evolution

The *in situ* stress evolution for the Ti/W multilayers is presented in Fig. 3(a). The stress-thickness product for all the films is plotted as a function of film thickness. The observations are as follows: First, all the multilayers exhibited the

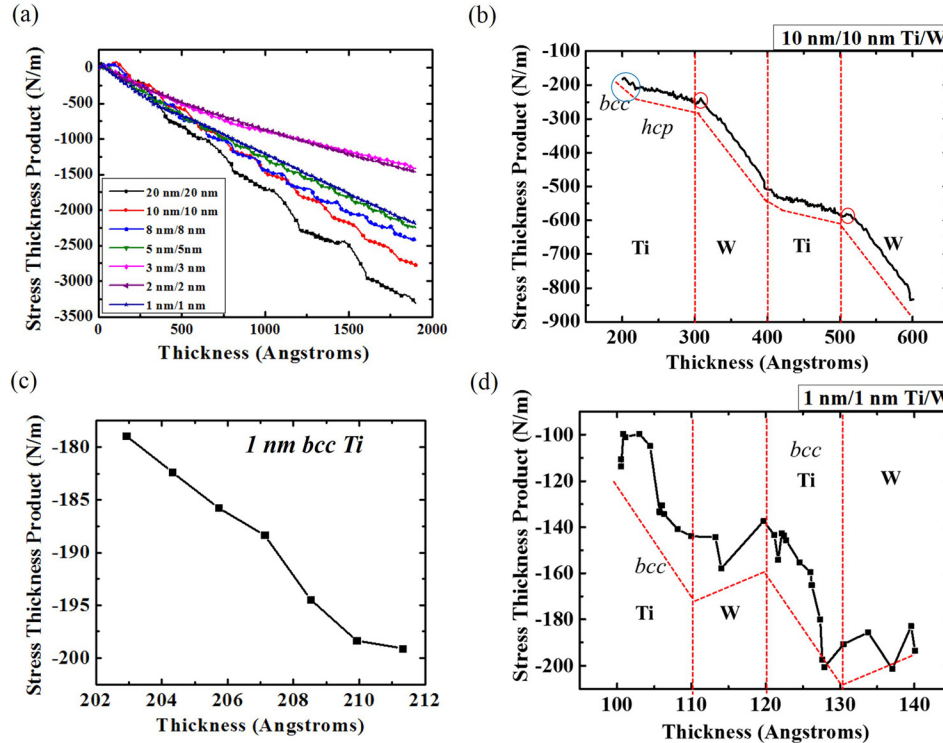


FIG. 3. (a) Stress evolution of the stress-thickness product versus thickness for various multilayers listed by their bilayer thickness. (b) Magnified stress-thickness product plot of the 10 nm/10 nm Ti/W multilayer. The inset reveals the large compressive stress slope for the first 1 nm of Ti growth. (c) The large compressive stress slope of the first 1 nm of Ti growth seen in (a). (d) Magnified stress-thickness product plot of the 1 nm/1 nm Ti/W multilayer.

overall compressive stresses in the post-coalescence regime,²³ which is consistent with the prior Ti/Nb behavior.¹⁴ Second, with a decreasing bilayer thickness, the overall stress became less compressive at an equivalent overall thickness among all hcp/bcc Ti/W multilayers. In contrast, Ti/Nb multilayers became even more compressive with decreasing bilayer thickness.¹⁴ Third, both the Ti and W layers in each multilayer have a compressive stress-thickness product slope. Of these two elements, W's compressive slope is much steeper than its Ti counterpart. And finally, for the 1 nm/1 nm multilayer, which adopted a single bcc phase, the compressive stress was recovered to values near that of the 5 nm/5 nm multilayer, e.g., this multilayer exhibited a much more compressive overall stress-thickness compression product than either the 3 nm/3 nm or 2 nm/2 nm multilayers.

The decrease of compressive stress slope with decreasing bilayer thickness among the hcp/bcc Ti/W multilayers is rationalized by a reduction of compressive interfacial stress, as tabulated in Table I. The measurement of interfacial stress was found by extrapolating the slope of the stress-thickness product data to zero thickness of the new layer and determining the difference between the absolute stress-thickness product value at the end of the old layer and that of the extrapolation back to zero thickness of the new layer.²⁸ The equation for interfacial stress measurement is shown below

$$\Delta_{\text{avg}} = [2 \cdot \Delta_{\text{Ti on W}}(<1 \text{ nm}) + (t_{\text{Ti}} - 1) \times \Delta_{\text{Ti on W}}(>1 \text{ nm}) + (\lambda - t_{\text{Ti}}) \cdot \Delta_{\text{W on Ti}}]/\lambda, \quad (3)$$

where t_{Ti} is the individual thickness of the Ti layer (nm) and λ is the bilayer thickness or $t_{\text{Ti}} + t_{\text{W}}$, $\Delta_{\text{Ti on W}}$ or when $\Delta_{\text{Ti on W}}$ in the respective thickness range.

In Table I, the interfacial stress is divided into two thickness regions, $\Delta_{\text{Ti on W}}(<1 \text{ nm})$ and $\Delta_{\text{Ti on W}}(>1 \text{ nm})$, for the

Ti growth based on the observed slope transition. The average interfacial stress for the bilayer was computed by weighting each interfacial value by its thickness. It can be observed that all multilayers studied in Table I have negative interfacial stress values (i.e., compressive interfacial stresses). The increasing interfacial stress value with bilayer thickness appeared to help driving the overall compressive behavior observed in these multilayers. It should be mentioned that the reported values are experimental measurements. As noted by Clemens *et al.*,⁴¹ interfacial intermixing can change the interfacial stress. In that work, the predicted calculations of the interfacial stress were altered by the extent of interface intermixing. Our equations described above are fitted to experimental measurements which accommodated whatever level of intermixing that may or may not be present in the multilayer. The STEM-HAADF image shown in Fig. 2(f) suggests no significant intermixing between the layers and will be further discussed in relationship to a MD simulation that predicted the phase transformation assuming no intermixing. The interfacial stress findings, coupled to the shifts in the XRD reflections of Fig. 1(a), suggest that each layer underwent some amount of

TABLE I. Interfacial stress values for various multilayers listed by their bilayer thicknesses.

Number	Bilayer thickness (nm)	Interfacial stress (N/m)			Average interfacial stress (N/m)
		$\Delta_{\text{Ti on W}}(<1 \text{ nm})$	$\Delta_{\text{Ti on W}}(>1 \text{ nm})$	$\Delta_{\text{W on Ti}}$	
1	20	-1.75	-0.4	-19.03	-9.78
2	16	-1.64	-16.39	7.09	-3.73
3	10	-1.27	-8.93	2.48	-2.28
4	4	0.24	3.98	-3.5	-0.65

strain accommodation, i.e., peak splitting, for the hcp Ti/bcc W layers. Consequently, the overall films were able to reduce their intrinsic compressive stress state with decreasing bilayer spacing. However, when the Ti layer underwent an hcp to bcc transition, the compressive stress of the collective film is increased indicating that the pseudomorphic stabilized phase is under a higher compressive stress state.

Figs. 3(b) and 3(d) are representative magnified stress-thickness product plots of 10 nm/10 nm and 1 nm/1 nm multilayers, respectively. In these images, one can understand how the stress evolved at each thickness as it grew and one can infer how structural stability may influence the measured values. For the films at 10 nm/10 nm thickness, the growth stress for the first 1 nm of Ti exhibited a large compressive behavior (steeper slope). Upon growing to thicknesses greater than ~ 1 nm, the Ti growth stress was slightly less compressive (gradual slope). A magnified image of the first 1 nm Ti stress behavior is plotted in Fig. 3(c). Based on the 1 nm stabilization of bcc Ti in the 1 nm/1 nm Ti/W multilayer, this change of slope could indicate the phase change.¹⁴

For the bcc Ti on W, with an orientation relationship of $(011)_\beta // (011)_{bcc} \mid \langle 111 \rangle_\beta // \langle 111 \rangle_{bcc}$, the coherency strain would be the following:

$$\varepsilon = \frac{d_{(011)_{Ti}} - d_{(011)W}}{d_{(011)}} = \frac{a_{Ti} - a_W}{a_{Ti}} = \frac{3.27 - 3.16}{3.27} \approx 3\%. \quad (4)$$

As the 1 nm bcc Ti grows on the W surface, such a misfit strain would result in a reduction of the interfacial energy by the removal of misfit dislocations. This would then contribute favorably towards a reduction in the interfacial energy contribution for stabilization discussed above,¹¹ albeit at the expense of volumetric strain energy increases. It is noteworthy that the *in situ* stress reflects the in-plane strain information. Since the stress shows a negative slope, which indicates a compressive nature, this would be in agreement that β -Ti has undergone in-plane compression to match W as given in Equation (4).

When the W layer grew on the hcp Ti surface, a small region (< 1 nm) of modest positive slope was noted in the stress response. This suggested an initial tensile growth condition as a very thin layer of W lattice matched itself to the Ti surface. This is shown by the circle region in Fig. 3(b) for the W film. Once the W film coalesced over the Ti surface, the W film revealed a much more compressive stress behavior than either the bcc or hcp Ti states. Though the mechanisms of compressive stress in the post-coalescence regime are still under investigation in the literature, it is accepted that this stress behavior can be related to the insertion of adatoms into the grain boundaries facilitating compression of the grains.^{18,19,21} The variation in data points within an individual layer shown in Fig. 3(d) was attributed to experimental noise or non-uniformity of deposition, i.e., drift in the detector, variation of the light source, thermal drift, etc.

How the phase change may play a role in the stress evolution can be inferred from the model proposed by Chason *et al.*²⁰ In this model, the growth stress is a function of the atomic volume, Ω , and is given as

$$\sigma_{ss} = \frac{\sigma_i \hat{R} - \sigma_0 [(\Delta\mu_0 + \delta\mu_s)/kT]}{\hat{R} + (\sigma_0 \Omega/kT)},$$

where σ_i is the stress before grain boundary formation, \hat{R} is the normalized growth rate for a particular grain height, σ_0 corresponds to the stress that would result if an additional adatom were added to the grain boundary without changing the size of the grain, $\Delta\mu_0$ corresponds to the differences between surface and grain boundary chemical potentials, $\Delta\mu_s$ is the increase in chemical potential from equilibrium during deposition, k is the Boltzmann constant, and T is the temperature. Clearly, a change in atomic volume will contribute to a change in stress. For hcp to bcc Ti, the atomic volume (in the reference's definition) changes from 11.76 \AA^3 (6 atoms in a unit cell, $V = a^2c$ ($\sin 60^\circ$)) to 34.97 \AA^3 (2 atoms in a unit cell, $V = a^3$). This is a nearly two-thirds volumetric increase which would have a notable effect on film stress. However, delineating its effects versus compounding other factors, such as adatom migration into grain boundaries, is compounded and is not easily obtained.

C. Atomistic simulation of phase transformation

To add further insights to the experimental results, MD simulations of Ti deposited onto a polycrystalline W substrate were performed and are presented in Fig. 4. The corresponding atoms are colored by either element type or crystal structure using the common neighbor analysis (CNA). Figs. 4(a), 4(c), and 4(e) are colored by element allowing for easier visualization of the W substrate and the Ti layer, whereas Figs. 4(b), 4(d), and 4(f) are colored by structure type using the CNA method. Fig. 4(h) is a schematic that represents the various regions and boundary conditions in the simulation as described in the modeling details found in Section II. At layer thicknesses at or less than 0.5 nm, the Ti revealed a bcc structure as shown in Fig. 4(b). As the thickness continued to thicken, the onset of hcp coordination initiated, evident by the very small volumes of destabilized regions of hcp Ti in the 1 nm layer, Figs. 4(c) and 4(d). Finally, at 2 nm of thickness, Figs. 4(e) and 4(f), the Ti layer is largely hcp. This is quantitatively captured on the hcp coordinated atom number plot versus thickness, Fig. 4(g), which showed the increasing hcp coordination configuration with increasing Ti film thickness.

The simulation does suggest a transition zone to the hcp phase initiating near 0.6 nm and completing near 1 nm of thickness, Fig. 4(g). One reason the experimental results may not show any hcp diffraction for the 1 nm/1 nm film could be either (1) a low volume fraction of the hcp phase was present but insufficient for the measurable diffracted intensities and/or (2) some amount of W intermixing with Ti during the deposition process which helped to stabilize the β -Ti phase. One could also argue that the top bcc W surface could be stabilizing the bcc Ti phase as well, since two bcc interfaces are now in contact with the Ti layer and contribute to the thermodynamic stabilization concepts proposed by Dregia *et al.*¹⁰ and described in Equation (2). However, the *in situ* stress revealed no discontinuity in the slope over the continuous bcc Ti growth thickness suggesting that bcc Ti is

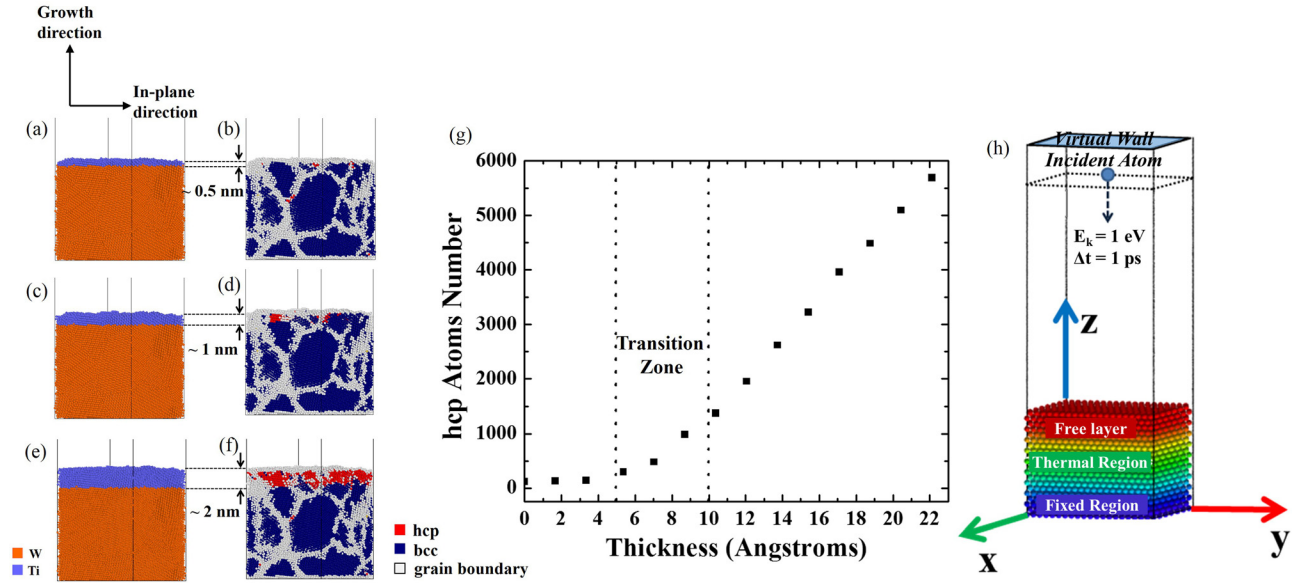


FIG. 4. The two sets of colors represent the atom types—Ti designation being purple and W designation being orange. The dark blue color represents the bcc atom coordination, red being the hcp atom coordination, and the gray being atoms with no long range coordinated structure, i.e., atoms at grain boundaries and surfaces (a) 0.5 nm of Ti on a W substrate. (b) 0.5 nm of bcc Ti grown on a bcc W. (c) 1 nm of Ti on W substrate. (d) 1 nm of bcc Ti grown on bcc W. (e) 2 nm of Ti on W substrate. (f) 2 nm of hcp Ti grown on bcc W. (g) Number of hcp coordinated atoms versus film thickness. (h) Schematic of simulation regions.

likely continuously stabilized up to 1 nm without this top W surface.

As observed in other systems¹⁴ and suggested above, intermixing can play an important role in stabilizing a pseudomorphic phase. The STEM-HAADF image in Fig. 2(f) revealed a reasonably pronounced layered morphology, even at the thinnest layers studied. The insignificant intermixing between the layers could be attributed to several factors, such as the following: The low homologous deposition temperature and low temperature solubility between the two species would not necessarily favor substantial mixing either kinetically or thermodynamically. The surface energy and crystallographic symmetry may not favor ease for mixing either. Zhou *et al.*³³ proposed and verified a sputter deposition mechanism where surface adatoms exchange with subsurface atomic layers to enrich the growth surface with the lowest surface energy species which led to growth dependent intermixing. Mezey and Giber⁴² reported that the surface energy ratio of γ_W/γ_{Ti} to be 1.4. Hence, it would be unlikely that incoming Ti adatoms would exchange with the prior W deposited subsurface layer since the lower surface energy species (Ti) is already present on the surface. Additionally, when Ti grows on a W surface, it experienced a compressive stress which would further hinder W's incorporation into the Ti layer. Based on the surface energy arguments, when W would be grown on the Ti surface, W should preferentially exchange with Ti to reduce its surface energy. However, hcp Ti has limited solubility for bcc W at room temperature, as indicated by its binary phase diagram.⁴³ Likewise W is a larger atom than Ti (146 pm vs. 136 pm, respectively⁴⁴) which would provide an additional mechanical strain for lattice incorporation. As a final point, from the binary phase diagram,⁴³ a miscibility gap exists under $\sim 1250^\circ\text{C}$ for the two bcc phases. This suggests that even when the two phases are the same symmetry, neither species has a strong tendency

to mix. Thus, for either the bcc/bcc or hcp/bcc multilayer cases of one layer growing on the other, one could rationalize that the no significant intermixing would be expected and explained the aforementioned cross-section micrographs in Fig. 2 of the 1 nm/1 nm layered structure. Attempts to perform atom probe tomography to further quantify the extent of atomic intermixing were undertaken. Unlike the prior report by the authors for Ti/Nb,¹⁴ these multilayers did not successfully field evaporate. The specimens continually fractured under voltage and laser pulsing which is attributed to the very large evaporation field differences between Ti and W.⁴⁵

IV. CONCLUSIONS

A series of Ti/W multilayered thin films with varying bilayer thicknesses have been sputter-deposited onto [001] Si substrates (with a native surface oxide on the substrate). As the bilayer thickness was reduced from 40 nm to 4 nm, the overall compressive stress reduced. Upon stabilizing bcc Ti for the 2 nm bilayer film (1 nm/1 nm), the compressive stress increased again to values commensurate with the 5 nm/5 nm bulk phase multilayer. This change in stress is attributed to the compressive stress state of the stabilized bcc/bcc phases. The growth of bcc Ti onto the W surface showed a steep compressive slope whose gradient decreased, but was still compressive, when compared to hcp Ti's growth. This discernable change in stress slope is believed to denote the bcc to hcp Ti transition as a function of Ti layer thickness. Cross-sectional transmission electron microscopy micrographs confirmed the layered morphologies even at the thinnest layers studied. The stress states for each film, during film growth, were rationalized by the lattice matching of the phase with the growth surface. The lattice strain and the reduction of interfacial energy are two key factors to drive

the bcc to hcp Ti phase transformation in the Ti/W multi-layers. These results were coupled to a molecular dynamics deposition simulation which revealed good agreement with the experimentally observed transformation thickness.

ACKNOWLEDGMENTS

The authors gratefully recognize the National Science Foundation, DMR-1207220 and the Central Analytical Facility in the University of Alabama for support. The authors also thank C.R. Weinberger for helpful technical discussions.

- ¹R. Hoogeveen, M. Moske, H. Geisler, and K. Samwer, *Thin Solid Films* **275**(1–2), 203 (1996).
- ²P. Boher, F. Giron, P. Houdy, P. Beauvillain, C. Chappert, and P. Veillet, *J. Appl. Phys.* **70**(10), 5507 (1991).
- ³W. Vavra, D. Barlett, S. Elagoz, C. Uher, and R. Clarke, *Phys. Rev. B* **47**(9), 5500(R) (1993).
- ⁴R. Q. Hwang and M. C. Bartelt, *Chem. Rev.* **97**(4), 1063 (1997).
- ⁵R. Koch, *J. Phys.: Condens. Matter* **6**(45), 9519 (1994).
- ⁶A. Miyamura, K. Kaneda, Y. Sato, and Y. Shigesato, *Thin Solid Films* **516**(14), 4603 (2008).
- ⁷C. Chuang, C. Chao, R. Chang, and K. Chu, *J. Mater. Process. Technol.* **201**(1), 770 (2008).
- ⁸R. Bruinsma and A. Zangwill, *J. Phys.* **47**(12), 2055 (1986).
- ⁹R. Bruinsma and A. Zangwill, *Europhys. Lett.* **4**(6), 729 (1987).
- ¹⁰S. Dregia, R. Banerjee, and H. Fraser, *Scr. Mater.* **39**(2), 217 (1998).
- ¹¹G. Thompson, R. Banerjee, S. Dregia, and H. Fraser, *Acta Mater.* **51**(18), 5285 (2003).
- ¹²G. Thompson, R. Banerjee, S. Dregia, M. Miller, and H. Fraser, *J. Mater. Res.* **19**(5), 707 (2004).
- ¹³J. Li, W. Liu, and Q. Jiang, *Acta Mater.* **53**(4), 1067 (2005).
- ¹⁴L. Wan, X. Yu, and G. B. Thompson, *Acta Mater.* **80**, 490 (2014).
- ¹⁵R. Cammarata, T. Trimble, and D. Srolovitz, *J. Mater. Res.* **15**(11), 2468 (2000).
- ¹⁶F. Spaepen, *Acta Mater.* **48**(1), 31 (2000).
- ¹⁷C. Friesen and C. Thompson, *Phys. Rev. Lett.* **89**(12), 126103 (2002).
- ¹⁸L. Freund and E. Chason, *J. Appl. Phys.* **89**(9), 4866 (2001).
- ¹⁹J. S. Tello, A. F. Bower, E. Chason, and B. W. Sheldon, *Phys. Rev. Lett.* **98**(21), 216104 (2007).
- ²⁰E. Chason, B. Sheldon, L. Freund, J. Floro, and S. Hearne, *Phys. Rev. Lett.* **88**(15), 156103 (2002).
- ²¹J. A. Floro, E. Chason, R. C. Cammarata, and D. J. Srolovitz, *MRS Bull.* **27**(01), 19 (2002).
- ²²G. Abadias, A. Fillon, J. J. Colin, A. Michel, and C. Jaouen, *Vacuum* **100**, 36 (2014).
- ²³A. González-González, C. Polop, and E. Vasco, *Phys. Rev. Lett.* **110**(5), 056101 (2013).
- ²⁴C. Pao, S. M. Foiles, E. B. Webb III, D. J. Srolovitz, and J. A. Floro, *Phys. Rev. Lett.* **99**(3), 036102 (2007).
- ²⁵J. W. Shin and E. Chason, *Phys. Rev. Lett.* **103**(5), 056102 (2009).
- ²⁶C. Taylor, D. Barlett, E. Chason, and J. Floro, *Ind. Phys.* **4**(1), 25 (1998).
- ²⁷G. G. Stoney, *Proc. R. Soc. London, Ser. A* **82**(553), 172 (1909).
- ²⁸A. L. Shull and F. Spaepen, *J. Appl. Phys.* **80**(11), 6243 (1996).
- ²⁹Y. Sasanuma, M. Uchida, K. Okada, K. Yamamoto, Y. Kitano, and A. Ishitani, *Thin Solid Films* **203**(1), 113 (1991).
- ³⁰L. Giannuzzi and F. Stevie, *Micron* **30**(3), 197 (1999).
- ³¹R. Johnson, *Phys. Rev. B* **39**(17), 12554 (1989).
- ³²H. N. G. Wadley, X. Zhou, R. A. Johnson, and M. Neurock, *Prog. Mater. Sci.* **46**(3–4), 329 (2001).
- ³³X. W. Zhou, H. N. G. Wadley, R. A. Johnson, D. J. Larson, N. Tabat, A. Cerezo, A. K. Petford-Long, G. D. W. Smith, P. H. Clifton, R. L. Martens, and T. F. Kelly, *Acta Mater.* **49**(19), 4005 (2001).
- ³⁴J. Li, *Modell. Simul. Mater. Sci. Eng.* **11**(2), 173 (2003).
- ³⁵A. Stukowski, *Modell. Simul. Mater. Sci. Eng.* **18**(1), 015012 (2010).
- ³⁶I. K. Schuller, *Phys. Rev. Lett.* **44**(24), 1597 (1980).
- ³⁷E. E. Fullerton, I. K. Schuller, H. Vanderstraeten, and Y. Bruynseraede, *Phys. Rev. B* **45**(16), 9292 (1992).
- ³⁸R. J. Kline, M. D. McGehee, and M. F. Toney, *Nat. Mater.* **5**(3), 222 (2006).
- ³⁹W. G. Burgers, *Physica* **1**(7–12), 561 (1934).
- ⁴⁰D. I. Potter, *J. Less-Common Met.* **31**(2), 299 (1973).
- ⁴¹B. Clemens, W. Nix, and V. Ramaswamy, *J. Appl. Phys.* **87**(6), 2816 (2000).
- ⁴²L. Mezey and J. Giber, *Jpn. J. Appl. Phys., Part 1* **21**(11), 1569 (1982).
- ⁴³J. Murray, *Bull. Alloy Phase Diagrams* **2**, 192 (1981).
- ⁴⁴J. E. Huheey, E. A. Keiter, and R. L. Keiter, “Inorganic chemistry: Principles of structure and reactivity” (Harper and Raw, New York, 1983).
- ⁴⁵M. K. Miller and R. G. Forbes, *Atom-Probe Tomography: The Local Electrode Atom Probe* (Springer, 2014).